

Fast Near-Surface Changes in the Defect Structure in Lithium Tetraborate Crystals in an External Electric Field

A. G. Kulikov^{a,*}, A. E. Blagov^{a,b}, N. V. Marchenkov^{a,b},
Yu. V. Pisarevskii^{a,b}, and M. V. Kovalchuk^{a,b}

^a *Shubnikov Institute of Crystallography, Federal Scientific Research Centre of Crystallography and Photonics, Russian Academy of Sciences, Moscow, 119333 Russia*

^b *National Research Centre Kurchatov Institute, Moscow, 123182 Russia*

**e-mail: ontonic@gmail.com*

Received April 14, 2020; revised July 11, 2020; accepted July 13, 2020

Abstract—The changes in the defect structure in the near-surface layers of lithium tetraborate ($\text{Li}_2\text{B}_4\text{O}_7$) single crystals under the influence of an external electric field applied along the polar direction [001] have been studied. Using the X-ray diffractometry with 2 ms time resolution the dynamics of the 004 and 008 diffraction peak parameters (the angular position and the integral intensity) variation was determined. Two types of processes caused by the redistribution of the charge localized at the surface of the polar dielectric and by the migration of lithium ions have been observed with different velocity and response time to the external field switching. The measurements are carried out at voltages at which the induced effects have reversible characters. The use of two orders of diffraction with different X-ray extinction lengths made it possible to visualize space charge layers near the anode and cathode by the intensity variation of the diffraction peaks. The estimation of the effective thickness of the charged near-surface layer gives the value of 25 μm for lithium ions at the cathode and about 45 μm for lithium vacancies at the anode.

Keywords: charge carriers migration, lithium tetraborate, time-resolved X-ray diffraction, external electric field

DOI: 10.1134/S1063783420120185

1. INTRODUCTION

Studying the processes of controlling functional characteristics of materials are of great interest for designing advanced systems of the data storage and energy accumulation. Usually, planar structures are used for this purpose. The possibility of formation of quasi-two-dimensional structures in dielectrics due to the charge carriers migration in an external electric field determines the interest to studying such processes in single crystals, too [1].

In strontium titanate (SrTiO_3) single crystals with the perovskite structure, the reversible process of changing the symmetry caused by a change in the oxygen vacancy concentration near the surface of the sample anode in the external high-strength electric field was observed and studied [2–4]. This process was observed as a broadening of diffraction reflection curves (DRC). Similar effects were also observed in paratellurite ($\alpha\text{-TeO}_2$) crystals as an electric field was applied in directions [110] and [100] [5–7]. In that case, two types of processes were observed. The first type is related to an increase in the lattice parameter due to vacancies outflow and takes place near the sample anode surface. Another type of the processes was

observed for both polarities of the applied electric voltage as the formation of slowly relaxing domains with a small angular disorientation due to a strong piezoelectric deformation.

The main studies in the abovementioned works were performed by the X-ray diffraction (XRD) method that enables one to obtain information on the transformation of the defect structure caused by the charge carriers migration. Similar X-ray diffraction pattern reflects the near-surface structural changes in the crystal lattice (distortions due to defects and phase transitions) caused by a transfer of coarse charge carriers (ions and vacancies) in dielectrics. Strontium titanate and paratellurite have low ionic conductivity at room temperature and close resistivity values $\rho = 10^{10} - 10^{11} \Omega \text{ m}$. Thus, the characteristic time (Maxwell relaxation time) of charge carriers migration and establishing the equilibrium state in electric field in these crystals is several hundred seconds, which made it possible to study the dynamics of the defect structure using the diffraction peaks measured by the traditional mechanical ω -scanning.

At the same time, there is a wide class of crystalline compounds, in which the changes in the structure due

to the migration of defect forming charge carriers (ions and vacancies) occur for the times of several milliseconds after switching-on an electric field [8], and the observation of the dynamics of the effects using the traditional X-ray diffraction method becomes impossible. Among such crystals is lithium tetraborate ($\text{Li}_2\text{B}_4\text{O}_7$), in which the effects of changing DRC in external electric field similar to the abovementioned were observed [9].

Recently the techniques and instruments that enable the study of the dynamics of structural changes by the registration of X-ray diffraction patterns with a milli- and even microsecond time resolution on a synchrotron radiation source [10] and a laboratory diffractometer [11, 12] have been developed. In this case, the technique is based on the influence of a periodic pulsed external electric field, which requires the reproducibility of the processes under the study and the relaxation to the initial state for some time after each pulse.

In this work, we studied the process of formation of quasi-two-dimensional structures caused by the migration of charge carriers (lithium ions) from the bulk to the near-surface region in the lithium tetraborate crystal in an external pulsed electric field applied in the direction of the polar tetrad axis. Because of the comparatively low resistivity ($\sim 10^8 \Omega \text{ m}$) and a small calculation Maxwell relaxation time, the measurements were carried out using the time-resolved X-ray diffraction method during a pulsed electric field influence on a sample.

2. LITHIUM TETRABORATE CRYSTALS

2.1. Properties

Lithium tetraborate was synthesized as a promising material for infrared transmitters [13, 14]. Later, it began to be used in gas analyzers [15], thermoluminescent dosimeters due to their pyroelectric properties [16, 17] and also in nonlinear optics, due to a wide pass band [18, 19]. In addition, lithium tetraborate is used in piezoengineering and acoustoelectronics [20, 21], since its piezoelectric moduli comparable with those of piezoceramics.

Lithium tetraborate crystals belong to the tetragonal system, space group $I4_1cd$ with lattice parameters $a = b = 9.479 \text{ \AA}$, $c = 10.286 \text{ \AA}$. The main structural elements of lithium tetraborate are boron–oxygen complexes (B_4O_9), consisting of two plane trigonal (BO_3) and two tetrahedral groups (BO_4), while lithium atoms are localized in interstitial sites [22, 23]. The main charge carriers are lithium ions [24]. The ionic conductivity of $\text{Li}_2\text{B}_4\text{O}_7$ is explained by lithium vacancies V_{Li}^- [25], since the high density of atomic packing and the stiffness of triangular and tetrahedral boron–oxygen polyhedral prevent direct jumps of lithium ions [26]. The lithium ions move through the one-dimen-

sion channel of the tetragonal axis [27]. The conductivity in the direction of polar axis [001] is almost five orders than that in the perpendicular directions [28].

The pyroelectric coefficient of $\text{Li}_2\text{B}_4\text{O}_7$ is most pronounced along direction [001] [29] and with a change in temperature from 50 to -150°C , changes from 30 to $120 \mu\text{C}/(\text{m}^2 \text{ K})$ [20]. The spontaneous polarization in lithium tetraborate at room temperature is $1.5 \mu\text{C}/\text{cm}^2$. As the electric field is applied along the tetrad axis [001], three components of the piezoelectric tensor $d_{31} = d_{32} = -2.0 \text{ pC/N}$ and $d_{33} = 20.4 \text{ pC/N}$ are active [30]. The dielectric permittivity is $\epsilon = 10.0$ [31].

2.2. Samples

The lithium tetraborate crystals studied in this work were grown from high-purity raw materials by the Czochralski method in platinum crucibles in an oxygen atmosphere. The obtained crystal was used to prepare the samples for the measurements, namely, single-crystal plane-parallel plates with linear sizes $13 \times 9 \times 0.55 \text{ mm}$ and a normal to the surface oriented in direction [001].

To remove the distorted layer, the preliminarily polished plates were subjected to chemical etching in the 50% HNO_3 solution. The continuous 30-nm-thick Ag contacts with 70-nm-thick Cr sublayer (for better adhesion with the crystal surface) were deposited on the prepared sample surfaces. The deposition was performed with a small (about 0.5 mm) margin from sample edges to prevent the formation of electric arc through the air.

2.3. Electrophysical Characteristics

The resistivity was measured using picoammeter (Keithley 6487). The electrical current was determined at the voltages up to 200 V on the sample plates. The results are shown in Fig. 1. The linear dependence of the current on voltage is conserved approximately to 40 V and the resistivity is $\rho = 7.8 \times 10^7 \Omega \text{ m}$. At high voltages, the electrical resistance decreased in time. In this case, a steady-state value of the current was achieved for hundreds seconds. The resulting resistivity was $1.7 \times 10^7 \Omega \text{ m}$ at the voltage of 200 V on the sample plates. The obtained values were used to calculate the Maxwell relaxation time $\tau_M = \epsilon_0 \epsilon \rho = 3 \text{ ms}$, where ϵ_0 is the dielectric constant.

3. TECHNIQUE

3.1. Technique of Time-Resolved X-ray Diffraction Measurements

The high-resolution double-crystal method of X-ray diffractometry enables one to determine and analyze the DRC parameters of a chosen reflection with high accuracy. The parameter of peak full width

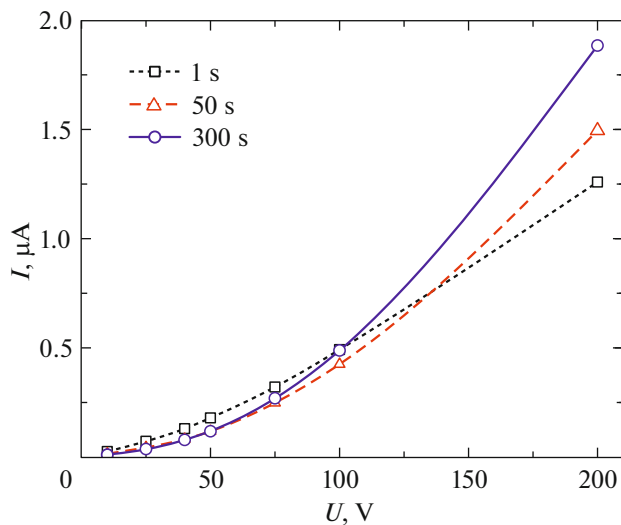


Fig. 1. Dependence of the electric current on the applied voltage at various delay times from the start of electric field application on the crystal.

at half maximum (FWHM) and the integral intensity (the sum over the angle of the elastic coherent diffraction component and inelastic diffusion scattering by defects) is one of the main characteristics of the crystal perfection. (The Bragg angle is related to the lattice parameter.) The variation of these parameters allows one to detect the changes in the real crystal structure [32–34].

The time-resolved technique of the double-crystal X-ray diffractometry under conditions of applying a

high-strength external electric field is described in detail in [11, 12]. DRC of a crystal is measured in the standard double-crystal geometry of the diffraction by ω -scanning of the sample. The system of a high-accuracy TTL synchronization based on the electric pulse generator (Tektronix) controls all equipment used in the experiment (Fig. 2): a multichannel intensity analyzer (ORTEC Easy-MCS), a high-voltage DC source, and a goniometer. For each angular position of a sample, the measurement cycle is started-up; during the cycle, at a certain instant of time, a high-voltage source (Matusada) feeds an electric field pulse of a given strength on the sample. The MCS analyzer enables one to separate the signal diffracted by the sample into short time intervals, the duration of which determines the real time resolution (up to 100 ns). On completion of the experiment, the obtained results are a set of the time dependences of the diffracted radiation intensities measured for each angular position of the sample in the conditions of identical acts of the external influence. Thus, the crystal state at each instant of time from the start of the cycle can be observed by changes in the DRC parameters.

It is important to note that the decisive advantage of the technique of studying fast processes in a single crystal used in this work is the possibility of determining the dynamics of all DRC parameters (position, integral and maximum intensities, and also the peak half-width). This circumstance distinguishes favorably this method from the method of fast measurement the intensity on the rocking curve slope [35] that can be used only at the condition of the invariant shape of the diffraction peak.

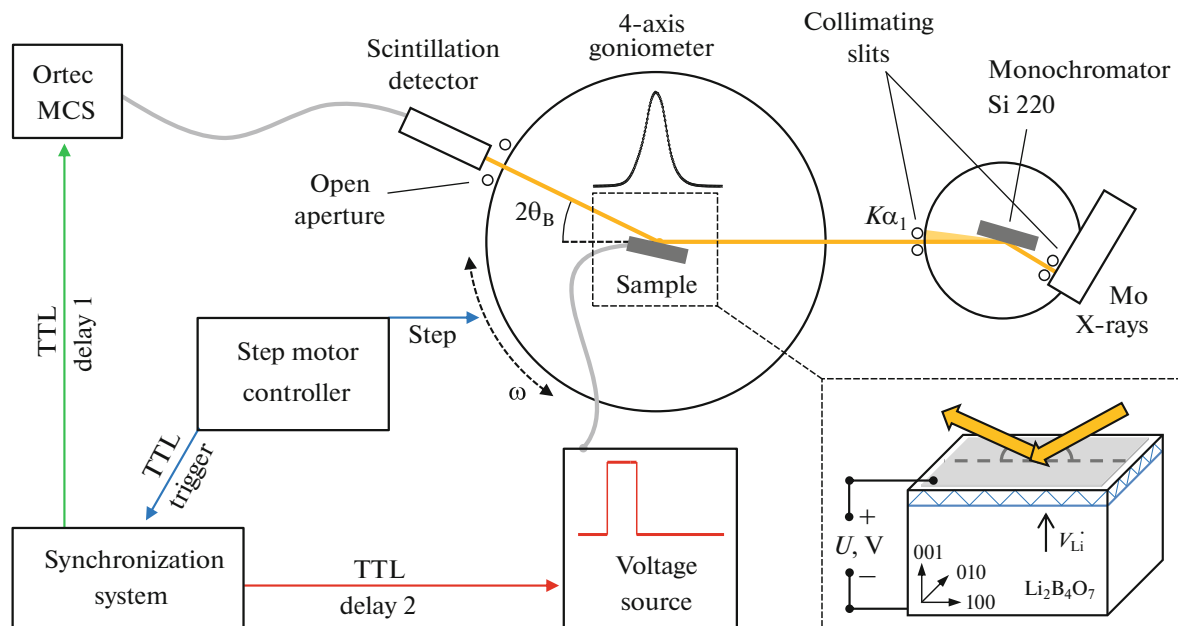


Fig. 2. The experimental setup of the time-resolved double-crystal diffractometry with multichannel detecting system.

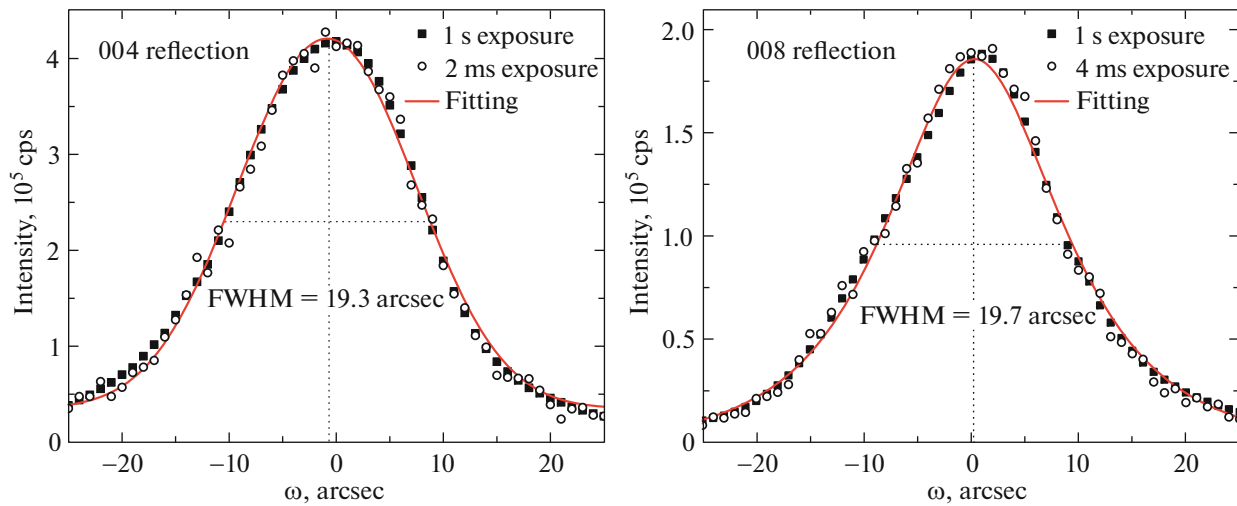


Fig. 3. DRC of reflections 004 and 008 of the lithium tetraborate crystal obtained with different time resolutions (exposure per one point). The line shows the DRC approximation by the analytic pseudo-Voigt function.

3.2. Experimental Equipment

The technique of time-resolved X-ray diffraction diagnostics is realized on the base of the laboratory instrument three-crystal X-ray spectrometer (TXS) [36, 37]. The setup (Fig. 2) was equipped with a precise goniometer for angular positioning in a step-by-step regime of scanning, which enables one to measure the DRC peaks in high-resolution conditions for further quantitative processing of the results. The radiation source was a molybdenum X-ray tube with wavelength of the $K\alpha_1$ line 0.70932 \AA and the power to 2.5 kW. The beam monochromatization was performed due to diffraction reflection 220 from a high-perfection Si crystal of the (110) cut and the 0.2–5-mm slits placed before the sample. The half-width of the proper DRC for the high-perfection Si 220 single crystal is 2.1829 arcsec . The radiation diffracted by the sample was measured by a Radicon scintillation detector with a dynamic range of intensity of $5 \times 10^5 \text{ cps}$. The slit before the detector was opened to accumulate a sufficient statistics in the peak.

3.3. Parameters of the Time-Resolved X-Ray Diffraction Experiment

The measurements were performed at the normal conditions and thermostating the experimental volume. 500 V pulses were applied on the sample, which corresponds to electric field strength 900 V/mm in the sample volume taking into account the crystal thickness. Since [001] is the polar direction, the measurements were performed for two signs of an external electric field, and the surface irradiated by the X-ray beam was the anode or cathode, respectively. The duration of the electric field pulses were 3 s long, since the changes in the defect structure occurring for this time are reproducible (reversible). For the complete

relaxation of the crystal to the initial state, the time between the pulses was significantly larger (about 1 min).

The experiments were carried out in the “reflection” geometry for two orders of symmetric reflection: 004 (the Bragg angle $\theta_B = 7.9^\circ$) and 008 ($\theta_B = 16.0^\circ$), for which the X-ray extinction lengths (L_{ext}) were $L_{\text{ext}} = 6.0 \text{ \mu m}$ and $L_{\text{ext}} = 34.1 \text{ \mu m}$, respectively.

The time resolution determined by the duration of one MCS channel was given from the limiting signal/noise ratio of the diffracted radiation, which is necessary for the adequate approximation of the whole data array by the analytical pseudo-Voigt function in the processing program written on the Python programming language. The peak profile form remains during the experiment (Fig. 3). The processing results were used to build the time dependences of the DRC approximation parameters: its angular position and integral intensity. We obtained the time resolution 2 ms for reflection 004 and 4 ms for reflection 008 having a lower reflection coefficient.

4. RESULTS

Figure 4 shows the three-dimensional distribution pattern of the intensity of the radiation diffracted by the sample in an angular vicinity of the exact Bragg position of reflection 004 for lithium tetraborate under the pulsed electric field with strength of -900 V/mm . This pattern corresponds to the full data array in the time–angle–intensity coordinates obtained during the experiment and describes the dynamics of changing DRC with the time resolution 2 ms.

Figure 5 presents the results of processing the experimental data: the angular dependences of the diffraction peak position for the positive and negative polarities, respectively. The colored region corre-

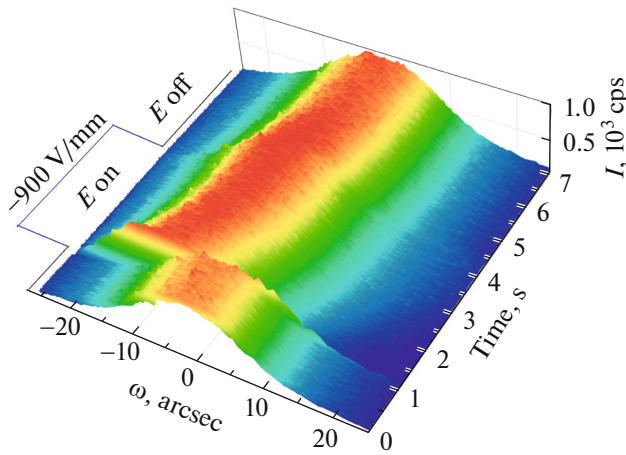


Fig. 4. Evolution of diffraction rocking curves (DRC) of 004 reflection in lithium tetraborate in the pulsed electric field with strength of 900 V/mm. The intensity distribution corresponding to the DRC peak is shown by the color. The time resolution is 2 ms. The electric field is switched-on at the first second of the cycle with duration of 60 s and is switched-off at the fourth second. The one-second delay before is used for the visualization of the stability of the crystal state. The cycle duration of 60 s is necessary for the crystal relaxation after the influence. The goniometer rotates to the following DRC point with a step of 0.5 arcsec in the cycle end.

sponds to the time interval during which the electric field is switched-on. It is seen that the change in the polarity leads to the change in the peak shift direction. However, at the initial instant of time after switching-on the field, the diffraction peak shifts to the same

direction for both polarities. This process has a reversible character. As the field is switched off, we observe a gradual relaxation of the crystal to the initial state.

Figure 6 shows the plots of the relative change in the integral intensity for both polarities. At the instant as the electric pulse is applied, the integral intensities of the peaks increases with subsequent relaxation to the initial state. The effect amplitude is maximal on the diffraction order with a smaller extinction lengths and at one (negative) polarity.

5. DISCUSSION

The reversible changes in the position (Figs. 5a, 5b) and also the integral intensity (Figs. 6a, 6b) of the diffraction maxima observed when the pulsed electric field act on the crystal are characteristic of the process of moving charged defects from the bulk to the near-surface region of the crystal [2–4], and the dynamics of this process is determined by Maxwell relaxation time. The changes in the both DRC parameters noted above give complimentary information on both the crystal lattice deformation and the defect structure in the crystal.

Similar characters and shifts of the diffraction maxima are observed for both orders of diffraction. Since DRCs were measured with the open slit ahead of the detector, the change in the angular position of the peak in axis ω is caused by the superposition of two changes: the rotation of atomic planes through angle $\Delta\omega_{\text{rot}}$ and contribution $\Delta\theta_d^{hkl}$ due to the change in the interplanar spacing $\Delta d/d$ along axis [001]. The angular

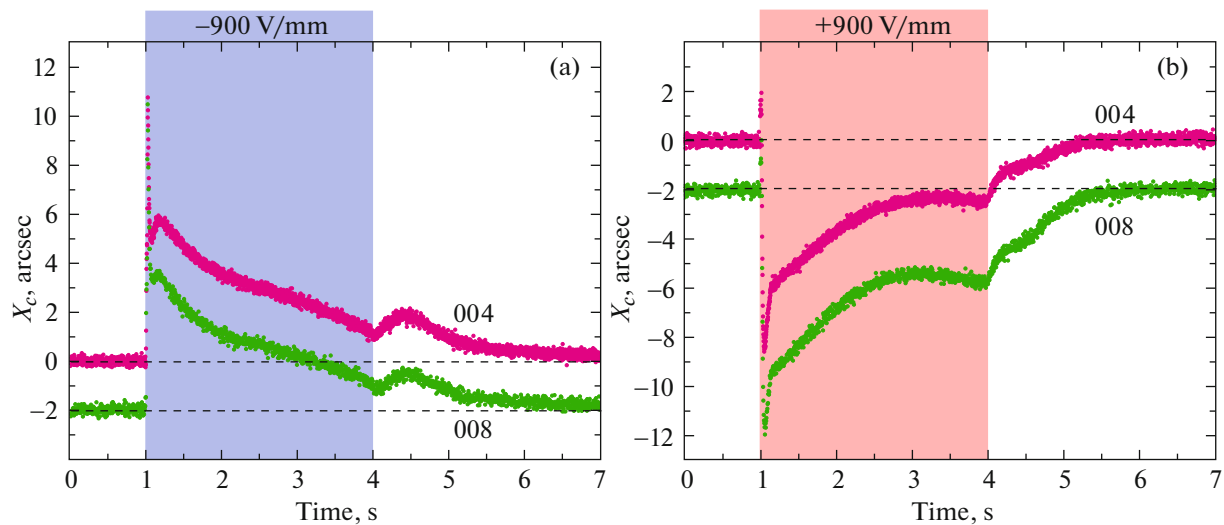


Fig. 5. Time dependences of the DRC peak position X_c along axis ω for reflection 004 ($L_{\text{ext}} = 6.0 \mu\text{m}$) and 008 ($L_{\text{ext}} = 34.1 \mu\text{m}$) under action of an external electric field with strength -900 V/mm of (a) the negative and (b) positive polarities on the sample. The field is switched-on at the first second and switched-off at the fourth second of the cycle. The position of the maximum for 008 is shifted by -2 for clarity. The area highlighted in color corresponds to the electric field pulse.

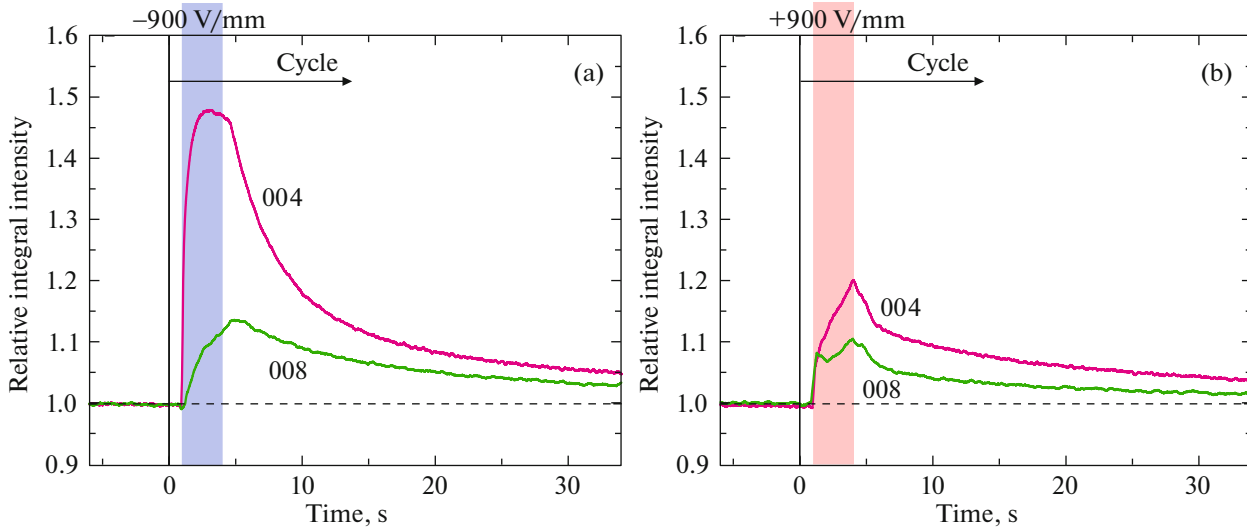


Fig. 6. Time dependencies of the integral intensities for two orders of the Bragg reflection: 004 ($L_{\text{ext}} = 6.0 \mu\text{m}$) and 008 ($L_{\text{ext}} = 34.1 \mu\text{m}$). The area highlighted in color corresponds to the electric field pulse.

shift of the experimental peak of $\Delta\theta_{\text{exp}}^{hkl}$ can be represented as the sum of two these quantities

$$\Delta\theta_{\text{exp}}^{hkl} = \Delta\theta_d^{hkl} + \Delta\omega_{\text{rot}}. \quad (1)$$

These two contributions can be separated from one another using the values of the Bragg angles θ_B^{hkl} of two chosen multiple reflections. As a result, the system of equations will be as follows

$$\frac{\Delta d}{d} = -\frac{\Delta\theta_d^{hkl}}{\tan\theta_B^{hkl}} = -\frac{\Delta\theta_{\text{exp}}^{008} - \Delta\theta_{\text{exp}}^{004}}{\tan\theta_B^{008} - \tan\theta_B^{004}}, \quad (2)$$

$$\Delta\omega_{\text{rot}} = \Delta\theta_{\text{exp}}^{004} + \frac{\Delta d}{d} \tan\theta_B^{004} = \Delta\theta_{\text{exp}}^{008} + \frac{\Delta d}{d} \tan\theta_B^{008}. \quad (3)$$

Consider the instant of the electric field switching in more detail. As seen from Figs. 7a, 7b, the main contribution to the peak shift is given by the bending deformations. Several time intervals can be distinguished. The dependences of the crystal lattice deformation have the specific features on these intervals T_1 and T_2 common for both polarities.

Interval T_1 (0–50 ms): the fast piezoelectric deformation of the crystal lattice as the electric field is switched-on and stabilized. For both polarities, the $\Delta d/d$ and $\Delta\omega_{\text{rot}}$ parameters demonstrate oscillations due to the redistribution of the charge induced near the polar crystal surface for the Maxwell time. The opposite-directed bending deformations appear in the crystal due to an electric field gradient near the surface (Fig. 7a). To the end of this time interval, we observe the stabilization of the parameters with the oppositely directed tensile–compression deformation $\Delta d/d$ (Fig. 7b).

Interval T_2 (>50 ms): during this interval, the formation of charged layers in the crystal near the electrodes is continued due to the migration of lithium ions Li^+ and lithium vacancies V_{Li}^- from the bulk. A V_{Li}^- layer is formed near the surface with a positive external potential (anode). The lattice parameter increases due to a strong piezoelectric deformation (Fig. 7b) with the steady-state value 5×10^{-5} . In the case of the field distribution homogeneous in thickness, the piezoelectric deformation (piezoelectric modulus d_{33}) is smaller and must be 1.9×10^{-5} [30]. Near the surface with a negative potential (cathode), a layer with increased Li^+ concentration in the crystal lattice, in which the parameter gradually increases. The oppositely directed bending deformations are also observed for both polarities (Fig. 7a).

Then, a partial screening of the external field is observed to the end of the electric pulse. After the electric field is switched off, the charge accumulated near the sample plate is gradually relaxed for a time no larger than the period of the pulse. The activation energy of lithium ions in $\text{Li}_2\text{B}_4\text{O}_7$ at room temperature is 0.35 eV [38]. The activation energy of oxygen vacancies is noticeably higher, about 1.65 eV, which corresponds to a lower conductivity over oxygen and significantly larger characteristic times of displacing oxygen vacancies in the crystal. The applying of a pulsed electric field (with the pulse duration 3 s) enables us to observe the dynamics of dominantly one type of charge carriers, namely, lithium ions.

The charge carriers aggregation causes the formation of a compensating electric layer with a high strength of the electric field in the near-surface region of the crystal with a thickness comparable to the X-ray

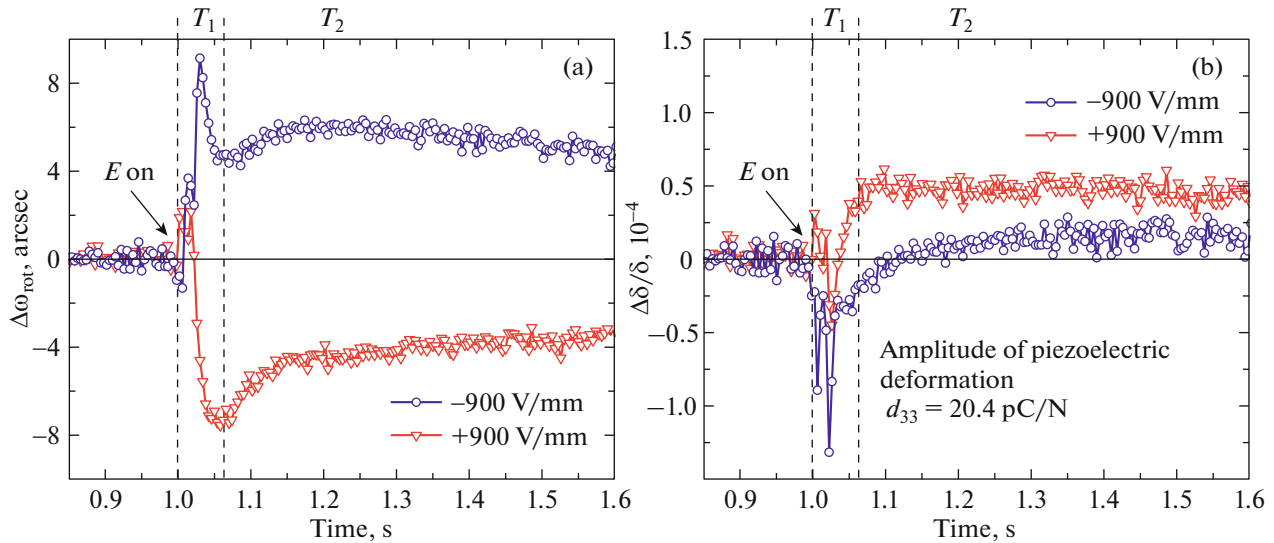


Fig. 7. (a) Dependences of the rotation angle of atomic planes $\Delta\omega_{\text{rot}}$ and (b) the change in the crystal lattice parameter $\Delta d/d$ calculated by two multiple diffraction orders 004 and 008 after the switching-on the electric field for the anode (red) and the cathode (dark blue). The positive value of the deformation $\Delta d/d$ corresponds to the crystal lattice extension, and the negative one, to its compression.

extinction length, i.e., about several tens of micrometers.

The measurements of the integral intensity (Fig. 6) on different orders of diffraction 004 and 008 more clearly characterize the defect concentration near the surface with averaging over a layer whose thickness is determined by the extinction. In this case, the effect is also sensitive to the polarity. The time dependence of changing the peak FWHM-parameter (it is not shown in figures) is identical to the integral intensity, which confirms the correlation of these parameters with the dynamics of the defect structure.

For the negative polarity (near cathode), the accumulation of the large number of Li^+ atoms in the near-surface region causes significant, about 50%, for reflection 004, increase in the integral intensity, which is three times higher than that for reflection 008. The time character of the increase is close to an exponential law. The characteristic time of the process is $\tau \approx 370 \text{ ms}$ for reflection 004, while, for reflection 008 with the extinction length larger by a factor of 5.6, the time of the process of ion accumulation $\tau \approx 1520 \text{ ms}$ due to a proportionally larger capacity of this layer.

At the same time, for the positive polarity corresponding to the anode, the accumulation of lithium vacancies V_{Li}^- in the near-surface region of the crystal also causes a change in the integral intensity of the reflections (about 10–20%) due to remained boron–oxygen complexes that deform the initial crystal lattice. In all above-mentioned cases, the charge relaxation after switching-off the field goes substantially longer.

Based on the differences in the integral intensities, we estimated qualitatively the charge distribution near the surface (Fig. 8). The calculations were carried out for the electrostatic case [39], in which the distribution of electric potential φ and induced charge density ρ on depth z obeys the law:

$$\varphi(z) = \varphi_0 e^{-\frac{z}{\lambda}}, \quad (4)$$

$$\Delta\varphi(z) = -\frac{1}{\varepsilon\varepsilon_0}\rho(z), \quad (5)$$

where φ_0 is the electric potential on the crystal surface, λ is the screening length, and Δ is the Laplace operator.

For the cathode, the estimation of the effective thickness of the charged layer λ gives the value $\sim 25 \mu\text{m}$, which is almost two times smaller than the effective layer thickness for the anode (about $45 \mu\text{m}$).

The results demonstrate the charge concentration near the surface on the cathode side and its more smoothed distribution near the crystal surface with the positive potential.

Significant differences in the kinetics of the integral intensities of DRC in the dependence on the diffraction reflection order and the polarity confirm different characters of near-surface charge regions formed in the crystal on the sides of the cathode and anode: a larger number of positively charged lithium ions and negatively charged BO_3 complexes, respectively.

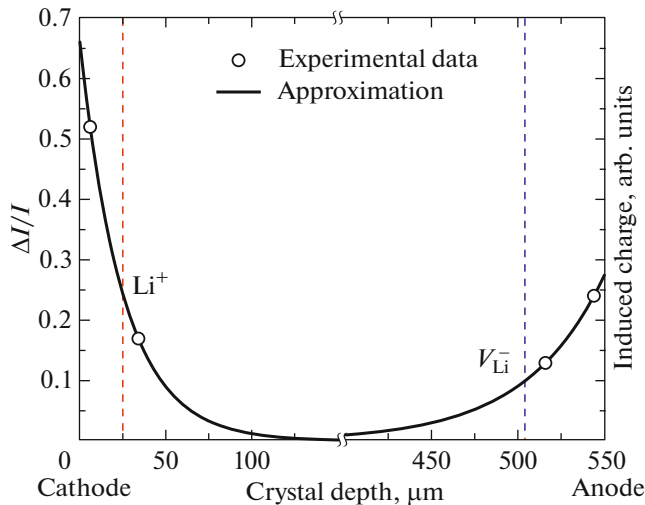


Fig. 8. (points) Change in the integral intensity $\Delta I/I$ of the reflections 004 and 008 with different extinction lengths and (solid line) the corresponding assumed distribution of the charge density in the near-surface crystal region caused by the migration of lithium ions. The approximation by the exponential function was performed, according to Eq. (5). The dashed lines show the effective thicknesses of charged layers.

6. CONCLUSIONS

The time-resolved X-ray diffraction technique made it possible to separate two types of the processes of changing in the defect structure differ in their kinetics' in the lithium tetraborate crystal in the pulsed electric field applied along the polar axis. One process with characteristic times of several tens of milliseconds is caused by the redistribution of free charge carriers near the surface induced due to the spontaneous polarization of the crystal. Another process with times of several seconds is related to the migration of charge carriers Li^+ and V_{Li}^- from the bulk and their localization near the surface. The characteristic times of the processes studied in this work are determined by high ionic conductivity of lithium tetraborate.

Using the time-resolved X-ray diffraction technique, we determined the thicknesses of the regions of the space charge localization in the layers near the both sample electrodes from the changes in the integral intensities of the diffraction peaks of two reflection orders in electric field of both polarities. The accumulation of the charge carriers (Li^+ and V_{Li}^-) near the sample surfaces for opposite polarities of the applied electric field agrees well with the observed differences in the changing of the defect structure.

ACKNOWLEDGMENTS

The authors are grateful to A.S. Il'in for the assistance in the electrophysical measurements and I.I. Atkinin for the assistance in the processing of the experimental data.

FUNDING

This work was supported by the Ministry of Science and Higher Education within the State assignment FSRC Crystallography and Photonics RAS in part of "crystal growth, sample preparation and data processing" and by the Russian Foundation for Basic Research (project 19-52-12029 NNIO_a) in part of "the development of the time-resolved technique and the studies of lithium tetraborate under the influence of electric field."

CONFLICT OF INTEREST

The authors declare that they have no conflicts of interest.

REFERENCES

1. Y. Watanabe, J. G. Bednorz, A. Bietsch, Ch. Gerber, D. Widmer, and A. Beck, *Appl. Phys. Lett.* **78**, 3738 (2001).
2. J. Hanzig, M. Zschornak, F. Hanzig, E. Mehner, H. Stöcker, B. Abendroth, C. Röder, A. Talkenberger, G. Schreiber, D. Rafaja, S. Gemming, and D. C. Meyer, *Phys. Rev. B* **88**, 024104 (2013).
3. J. Hanzig, M. Zschornak, E. Mehner, F. Hanzig, W. Münchgesang, T. Leisegang, H. Stöcker, and D. C. Meyer, *J. Phys.: Condens. Matter* **28**, 225001 (2016).
4. B. Khanbabae, E. Mehner, C. Richter, J. Hanzig, M. Zschornak, U. Pietsch, H. Stöcker, T. Leisegang, D. C. Meyer, and S. Gorfman, *Appl. Phys. Lett.* **109**, 222901 (2016).
5. M. V. Kovalchuk, A. E. Blagov, A. G. Kulikov, N. V. Marchenkov, and Yu. V. Pisarevsky, *Crystallogr. Rep.* **59**, 862 (2014).
6. A. G. Kulikov, A. E. Blagov, N. V. Marchenkov, V. A. Lomonov, A. V. Vinogradov, Yu. V. Pisarevsky, and M. V. Kovalchuk, *JETP Lett.* **107**, 646 (2018).
7. A. G. Kulikov, A. E. Blagov, A. S. Ilin, N. V. Marchenkov, Yu. V. Pisarevsky, and M. V. Kovalchuk, *J. Appl. Phys.* **127**, 065106 (2020).
8. A. K. Ivanov-Shits and I. V. Murin, *Solid State Ionics* (SPb Univ., St. Petersburg, 2000), Vol. 1 [in Russian].
9. A. G. Kulikov, Yu. V. Pisarevskii, A. E. Blagov, N. V. Marchenkov, V. A. Lomonov, A. A. Petrenko, and M. V. Koval'chuk, *Phys. Solid State* **61**, 548 (2019).
10. S. Gorfman, O. Schmidt, M. Ziolkowski, M. von Kozierowski, and U. Pietsch, *J. Appl. Phys.* **108**, 064911 (2010).
11. N. V. Marchenkov, A. G. Kulikov, A. A. Petrenko, Yu. V. Pisarevsky, and A. E. Blagov, *Rev. Sci. Instrum.* **89**, 095105 (2018).
12. N. V. Marchenkov, A. G. Kulikov, I. I. Atkinin, A. A. Petrenko, A. E. Blagov, and M. V. Kovalchuk, *Phys. Usp.* **62**, 179 (2019).
13. J. D. Garrett, M. NatarajanIyer, and J. E. Greedan, *J. Cryst. Growth* **41**, 225 (1977).
14. D. Robertson and I. Young, *J. Mater. Sci.* **17**, 1729 (1982).
15. R. Mohandoss, S. Dhanuskodi, B. Renganathan, and D. Sastikumar, *Curr. Appl. Phys.* **13**, 957 (2013).

16. I. Ketsman, D. Wooten, J. Xiao, Ya. B. Losovyj, Ya. V. Burak, V. Adamiv, A. Sokolov, J. C. Petrosky, J. W. McClory, and P. A. Dowben, *Phys. Lett. A* **374**, 891 (2010).
17. J. H. Schulman, R. D. Kirk, and E. J. West, in *Proceedings of the International Conference on Luminescence Dosimetry, Stanford, June 1965*, CONF-650637 (Clearinghouse, Springfield, 1967), OCLC 841357796, p. 113.
18. S. Furusawa, O. Chikagawa, S. Tange, T. Ishidate, H. Orihara, Y. Ishibashi, and K. Miwa, *J. Phys. Soc. Jpn.* **60**, 2691 (1991).
19. R. Komatsu, T. Sugawara, K. Sassa, N. Sarukura, Z. Liu, S. Izumida, Y. Segawa, S. Uda, T. Fukuda, and K. Yamanouchi, *Appl. Phys. Lett.* **70**, 3492 (1997).
20. A. S. Bhalla, L. E. Cross, and R. W. Whatmore, *Jpn. J. Appl. Phys.* **24**, 727 (1985).
21. R. W. Whatmore, N. M. Shorrocks, C. O'Hara, F. W. Ainger, and I. M. Young, *Electron. Lett.* **17**, 11 (1981).
22. C. V. Radaev, L. A. Muradyan, L. F. Malakhova, Ya. V. Burak, and V. I. Simonov, *Sov. Phys. Crystallogr.* **34**, 842 (1989).
23. L. Hanbin, S. Guangqiu, W. Xiaoqing, W. Jingzhi, and S. Denzhong, *Prog. Cryst. Growth Charact.* **40**, 235 (2000).
24. A. E. Aliev, Ya. V. Burak, and I. T. Lyseiko, *Izv. Akad. Nauk SSSR, Ser. Neorg. Mater.* **26**, 1991 (1990).
25. C.-S. Kim, D. J. Kim, Y.-H. Hwang, H. K. Kim, and J. N. Kim, *J. Appl. Phys.* **92**, 4644 (2002).
26. I. M. Rizak, V. M. Rizak, N. D. Baisa, V. S. Bilanich, M. V. Boguslavskii, S. Yu. Stefanovich, and V. M. Golovei, *Crystallogr. Rep.* **48**, 676 (2003).
27. M. M. Islam, T. Bredow, and C. Minot, *Phys. Chem. B* **110**, 17518 (2006).
28. C.-S. Kim, Y. H. Hwang, H. K. Kim, and J. N. Kim, *Phys. Chem. Glass.* **44**, 166 (2003).
29. V. T. Adamiv, Y. V. Burak, D. J. Wooten, J. McClory, J. Petrosky, I. Ketsman, J. Xiao, Y. B. Losovyj, and P. A. Dowben, *Materials* **3**, 4550 (2010).
30. I. M. Sil'vestrova, P. A. Senyushchenkov, V. A. Lomonov, and Yu. V. Pisarevskii, *Sov. Phys. Solid State* **31**, 1836 (1989).
31. S. Furusawa, S. Tange, Y. Ishibashi, and K. Miwa, *J. Phys. Soc. Jpn.* **59**, 2532 (1990).
32. V. Holy and J. Kubena, *Phys. Status Solidi B* **151**, 23 (1989).
33. V. G. Baiyakhtar, M. V. Kovalchuk, Yu. M. Litvinov, V. B. Molodkin, V. V. Nemoshkalenko, S. I. Olikhovskii, E. N. Kislovskii, and A. I. Nizkova, *Nucl. Instrum. Methods Phys. Res., Sect. A* **308**, 291 (1991).
34. M. G. Tsoutsouva, V. A. Oliveira, J. Baruchel, D. Camel, B. Marie, and T. A. Lafford, *J. Appl. Crystallogr.* **48**, 645 (2015).
35. S. Annaka, *J. Appl. Crystallogr.* **10**, 354 (1977).
36. M. V. Koval'chuk, E. K. Kov'ev, Yu. M. Kozelikhin, A. V. Mirenskii, and Yu. N. Shilin, *Prib. Tekh. Eksp.*, No. 1, 194 (1976).
37. A. E. Blagov, N. V. Marchenkov, Yu. V. Pisarevsky, P. A. Prosekov, and M. V. Kovalchuk, *Crystallogr. Rep.* **58**, 49 (2013).
38. L. Bohaty, S. Haussuhl, and J. Liebertz, *Cryst. Res. Technol.* **24**, 1159 (1989).
39. V. L. Bonch-Bruevich and S. G. Kalashnikov, *Semiconductors Physics* (Nauka, Moscow, 1977) [in Russian].

Translated by Yu. Ryzhkov